Astronomy & Astrophysics

Relation between metallicities and spectral energy distributions of Herbig Ae/Be stars

A potential link with planet formation

J. Guzmán-Díaz[1], B. Montesinos[1], I. Mendigutía[1], M. Kama[2], G. Meeus[3], M. Vioque[4,5],
R. D. Oudmaijer[6], and E. Villaver[1]

[1] Centro de Astrobiología (CSIC-INTA), ESA-ESAC Campus, Camino Bajo del Castillo s/n, 28692, Villanueva de la Cañada, Madrid, Spain
e-mail: jguzman@cab.inta-csic.es

[2] Department of Physics and Astronomy, University College London, Gower Street, London, WC1E 6BT, UK

[3] Departamento Física Teórica, Facultad de Ciencias, Universidad Autónoma de Madrid, Campus de Cantoblanco, Carretera Colmenar s/n - km 15, 28049, Madrid, Spain

[4] Joint ALMA Observatory, Alonso de Córdova 3107, Vitacura, Santiago 763-0355, Chile

[5] National Radio Astronomy Observatory, 520 Edgemont Road, Charlottesville, VA 22903, USA

[6] School of Physics and Astronomy, University of Leeds, Leeds LS2 9JT, UK

ABSTRACT

Context. Most studies devoted to Herbig Ae/Be stars (HAeBes) assume solar metallicity. However, the stellar metallicity, [M/H], is a fundamental parameter that can strongly differ depending on the source and may have important implications for planet formation. It has been proposed that the deficit of refractory elements observed in the surfaces of some HAeBes may be linked to the presence of cavities in their disks and is likely caused by Jovian planets that trap the metal-rich content.
Aims. This work aims to provide a robust test on the previous proposal by analyzing the largest sample of HAeBes characterized by homogeneously derived [M/H] values and stellar and circumstellar properties.
Methods. The spectra of 67 HAeBes, along with their well-known properties drawn from our previous work, have been collected from the ESO Science Archive Facility. Their [M/H] values were derived based on the comparison with Kurucz synthetic models. Statistical analyses were carried out with the aim to test the potential relation between [M/H] and the Meeus group I sources, with spectral energy distributions (SEDs) associated with the presence of cavities potentially carved by giant planets. We critically analyzed the eventual link between [M/H], the SED groups, and the presence of such planets.
Results. Our statistical study robustly confirms that group I sources tend to have a lower [M/H] (typically ~ -0.10) than that of group II HAeBes ($\sim +0.14$). A similar analysis involving SED-based transitional disks, with infrared excess only at wavelengths of ≥ 2.2 μm, does not reveal such a relation with [M/H]. This result indicates that not all processes capable of creating holes in the inner dust disks end up having an effect on the stellar abundances. The spatial distributions of group I and II sources are similar, at least within the available range of distances to the galactic centre and the galactic plane, for which the observed [M/H] differences are not driven by environmental effects. In addition, group I sources tend to have stronger (sub-) mm continuum emission presumably related to the presence of giant planets. Indeed, literature results indicate that disk substructures probably associated with the presence of giant planets are up to ten times more frequent in group I HAeBes than in group II. Finally, along with the metallicities derived for the whole sample, surface gravities and projected rotational velocities are additional outcomes reported in this work.
Conclusions. We provide indirect evidence to suggest that giant planets are more frequent around group I/low [M/H] stars than around the rest of the HAeBes. However, a direct test of the previous hypothesis requires multiple detections of forming planets in their disks. Such detections have so far been limited to the candidate around the metal depleted ([M/H] $= -0.35 \pm -0.25$) group I HAeBe star AB Aur, which is consistent with our findings.

Key words. protoplanetary disks – planet-disk interactions – stars: pre-main sequence – stars: variables: T Tauri, Herbig Ae/Be – stars: fundamental parameters

1. Introduction

Stellar metallicity, [M/H][1], may be a factor that plays a fundamental role in planet formation. Soon after the discovery of the first exoplanets around solar-type stars, a trend linking the presence of planets to stars with higher [M/H] values became apparent (Gonzalez 1997; Santos et al. 2000, 2001). As the number of detected exoplanets increased, further evidence confirmed and strengthen the today well-known "planet-metallicity" correlation for FGK stars (see, e.g., Adibekyan 2019; Osborn & Bayliss 2020, and references therein). However, the case of A-type stars is still far from clear. Less than 20 planets have been confirmed around stars with effective temperatures between 8000 and 12 000 K[2], which makes a robust statistical study unfeasible at this stage. Indeed, the most common methods for

---

[1] [M/H] is defined as $\log[N_M/N_H]_{star} - \log[N_M/N_H]_\odot$, N_M and N_H being the abundances of all elements heavier than hydrogen and helium, and the abundance of hydrogen, respectively.

[2] http://exoplanet.eu/

detecting exoplanets are based on weak spectroscopic velocity signals and photometric transits, for which the relatively small number of photospheric signatures (typically large rotational velocities and high luminosities of hot stars) make them difficult targets to probe.

Concerning the precursors of main-sequence A and B stars, recent studies have been carried out to characterize large samples of young, intermediate-mass Herbig Ae/Be objects (HAeBes, Vioque et al. 2018; Arun et al. 2019; Wichittanakom et al. 2020; Guzmán-Díaz et al. 2021) and to significantly increase the number of potential members belonging to the class (Vioque et al. 2020, 2022; Zhang et al. 2022; Kuhn et al. 2023). However, most studies devoted to HAeBes do not usually analyze [M/H] and the solar value is adopted by default. Only a handful of works have considered the chemical peculiarities that HAeBes can show (such as the λ Boötis phenomenon; see e.g., Gray & Corbally 1998), determining abundances for relatively small sub-samples (e.g., Acke & Waelkens 2004; Guimarães et al. 2006; Montesinos et al. 2009; Folsom et al. 2012).

A major study involving [M/H] in HAeBes was carried out by Kama et al. (2015). These authors proposed that the HAeBes showing a deficit of refractory elements and, thus, low values of [M/H] could be linked to the presence of Jupiter-like size exoplanets in their protoplanetary disks. This scenario does not necessarily imply that A and B stars harboring giant planets are globally metal-poor, which would be in opposition to the planet-metallicity correlation found in late-type stars. According to Kama et al. (2015), planets undergoing formation mainly trap the metal-rich material, with the remaining accreted by the central star being metal-depleted. Given that A and B stars have radiative envelopes, the mixing timescale with the interior is on the order of ~Myr, much slower than that for lower mass stars with convective sub-photospheric regions. Therefore, [M/H] measurements in HAeBes refer to freshly accreted material and only reflect the stellar surfaces. Additional details on the theoretical model behind the previous scenario are described in Jermyn & Kama (2018), and similar views proposed to explain the properties of some post-AGB stars and solar twins can be consulted, for instance, in Oomen et al. (2019), Booth & Owen (2020), Kluska et al. (2022), and references therein. Other scenarios involving changes in the stellar metallicity have been explored, for instance, in the context of stars with planets and debris disks (Maldonado et al. 2012, 2015) or on galactic scales (e.g., Adibekyan et al. 2014; Hawkins 2022, and references therein).

On the other hand, the proposal from Kama et al. (2015) hinges on the fact that the deficit in [M/H] is observed in stars belonging to group I in the classification by Meeus et al. (2001). This is based on the shape of the spectral energy distribution (SED) in the infrared and submillimeter regions. Such a classification has been related (among others properties) with the morphology of the circumstellar disks, where group I and group II sources are associated with "flared" and self-shadowed, "flattened" disks, respectively (e.g., Meeus et al. 2001; Dullemond 2002; Dullemond & Dominik 2004). Demonstrating what is most relevant to the hypothesis by Kama et al. (2015), studies based on high-resolution imaging suggest that disks belonging to group I sources show cavities potentially carved out by giant planets (e.g., Maaskant et al. 2013; Honda et al. 2015; Garufi et al. 2017; Stapper et al. 2022).

Although the scenario proposed by Kama et al. (2015) could have major implications for our understanding of planet formation, it was based on a study of a relatively small sample of 22 HAeBes. In fact, these were the only ones having measured

[M/H] values and disk structure classification from SEDs by that time, which were based on heterogeneous studies from the literature. Our main aim is to solve these issues by providing a robust test on whether the [M/H] of HAeBes can be related to a specific SED-based disk structure from the Meeus et al. (2001) scheme or not. Given that the answer we find is affirmative, the potential implications in terms of the presence of giant planets are further analyzed. The departure point is our previous work in Guzmán-Díaz et al. (2021), where the stellar parameters and the circumstellar morphology in terms of the Meeus et al. (2001) groups were homogeneously derived for essentially all classical, historically well-known HAeBes. Here, we derive [M/H] for all such objects for which this parameter can be measured from suitable spectra, extending the sample analyzed by Kama et al. (2015) by a factor ~3. On top of the new [M/H] values for all the stars, projected rotational velocities ($v \sin i$) and surface gravities ($\log g$) will also be provided as valuable outcomes of our work. Section 2 describes the sample and the observations. The process to estimate [M/H] and the rest of stellar parameters is described in Sect. 3. An analysis of the previous results is in Sect. 4, which includes a statistical study and discussion regarding the connection between [M/H] and the SED classification. Finally, a brief summary and our main conclusions are given in Sect. 5.

2. Sample and observations

We started by selected an initial sample of HAeBes with effective temperatures, $T_{\rm eff}$, below 12 000 K (spectral types later than B8) from Guzmán-Díaz et al. (2021) and with one-dimensional (1D) spectra available at the ESO Science Archive Facility[3]. Accordingly, the stellar mass ranges typically between 1 and 5 $M_\odot$ and the ages are mostly <15 Myr. We discarded emission-dominated stars that do not show enough absorption lines (i.e., mainly HBe stars with $T_{\rm eff} > 12 000$ K). Sources with spectra that do not have a high enough signal-to-noise ratio (S/N typically ≥100 for all stars except for four listed in Appendix B, with $S/N \geq 50$) or spectral resolution (see below) were also discarded. The final sample is comprised of 67 sources, whose main properties are summarized in Table A.1. All data listed in that table were compiled from the photometric study of Guzmán-Díaz et al. (2021), except for the spectroscopically determined $T_{\rm eff}$ values taken from Wichittanakom et al. (2020), whenever available. The final sample covers a range of luminosities – in $\log(L_*/L_\odot)$ – between 0.4 and 3.2, masses between 1.4 and 7.0 $M_\odot$, and ages between 0.2 and 20 Myr, representing almost 50% of all classical, late-type HAeBes studied in Guzmán-Díaz et al. (2021). Regarding the SEDs studied in that work, 28 sources were classified as group I and 34 as group II. Although five stars could not be classified with regard to the SED groups, they have also been included in the current sample for completeness, given that their [M/H] values could also be determined from the available spectra.

Most spectra in this study were taken with the X-shooter/VLT spectrograph. The spectral resolution, $R = \lambda/\Delta\lambda$, varies between ~3200 and ~18 400 depending on the wavelength range and the slit width. Spectra taken with UVES/VLT and HARPS/La Silla 3.6-m, were also used, with $R \sim 41\,000-110\,000$ and ~80 000−115 000, respectively. Finally, the spectrum of HBC 222 was taken with GIRAFFE/VLT ($R \sim 5500-65\,000$). The spectrographs used to obtain the spectra of each source, and their resolution measurements at ~5000 Å are listed in Cols. 2 and 3 of Table A.2. The first

---

[3] http://archive.eso.org/cms/html

initials indicate the instruments and resolutions corresponding to the spectra used to estimate $v \sin i$, and the second to those used for measuring the widths of the Balmer lines (i.e., $\log g$) and [M/H] (see Sect. 3). In the case where several spectra from the same instrument were available for a given star, priority was given to the one with the highest spectral resolution.

The spectra used in this work are the final products of the processing of the raw data – and the corresponding calibration files – through the pipelines developed by the instruments' teams. Special care was taken to normalize the spectra; narrow regions free from lines were chosen in the original spectra and the mean intensities of each small interval were used as clips to build a full continuum using cubic splines. The RASSINE program (Cretignier et al. 2021) has been used in automatic mode to improve the normalization of a few UVES and HARPS spectra. Telluric contamination in our spectra is significant within the ranges of ~5850–6000 Å and ~6450–6600 Å, but these ranges are not used in the analysis (Sect. 3). Therefore, although telluric correction was not applied this does not affect our results.

3. Results

This section describes how the [M/H] values were obtained from the comparison of the observed spectra with photospheric models, with $v \sin i$ and $\log g$ additional outcomes of the process. Synthetic Castelli-Kurucz spectra computed with the suite of codes ATLAS9 (Castelli & Kurucz 2003) were used throughout. These models do not consider disk-to-star accretion, which can produce a continuum excess – and possible line veiling in the coldest sources – mainly at wavelengths shorter than studied in this work (e.g., Muzerolle et al. 2004; Mendigutía et al. 2011, 2014).

3.1. Projected rotational velocities

The first step was to estimate the $v \sin i$ of each star. Although the derivation of [M/H] does not strictly depend on the $v \sin i$ values – as rotation does not have an effect on equivalent width, which is extensively used throughout this work (see Sect. 3.2) – this parameter facilitates the visual comparison between observations and models.

Before describing the procedure for estimating $v \sin i$, some words of caution are pertinent. In some cases, when the resolution of the spectrograph is not particularly high (say, below 30 000) this parameter puts some limits to the estimated values of $v \sin i$. The widths of some telluric or arc lines give an idea of the instrumental response of the spectrograph; we may use σ_{inst} to refer to that value. Assuming Gaussian profiles, the actual stellar line profiles with widths, σ_{real}, and the instrumental σ_{inst} can be combined according to the expression $\sigma_{\text{obs}}^2 = \sigma_{\text{inst}}^2 + \sigma_{\text{real}}^2$, where "obs" stands for "observed." For the case where $\sigma_{\text{real}} = 2\,\sigma_{\text{inst}}$, we would have $\sigma_{\text{obs}} = \sqrt{5}\,\sigma_{\text{inst}}$. Identifying $\sigma \equiv v$, namely, widths and velocities, the relative error $(v_{\text{obs}} - v_{\text{real}})/v_{\text{real}}$ would be ~11%. For the particular case of all the X-shooter spectra obtained with $R = 9900$, $\sigma_{\text{inst}} \simeq 30$ km s^{-1}, that is, values of $v \sin i$ below twice the aforementioned value would be affected by larger uncertainties and must be taken as upper limits, with the situation becoming more critical for the few stars whose spectra were obtained with even lower resolutions.

The broad, isolated Mg II feature at 4481 Å was generally used to estimate the $v \sin i$ of the objects. For each star, the full width at half depth (FWHD) of that line was varied by changing the $v \sin i$ in the synthetic model with the corresponding T_{eff} from Table A.1. The $v \sin i$ that provided a FWHD equal to that of

the observed spectra within 5% was adopted as the final value. Column 4 of Table A.2 lists the $v \sin i$ values obtained for the sample stars. Alternative photospheric lines were used for the few stars showing a Mg II line with a peculiar profile that makes the estimation of $v \sin i$ challenging. In addition, previous $v \sin i$ values from the literature were taken as a departure point and refined based on the procedure described above for the following stars: CO Ori (Herbig & Bell 1988; Mora et al. 2001; Glebocki & Gnacinski 2005), HBC 217 (McGinnis et al. 2018), HBC 222 (McGinnis et al. 2018), HD 101412 (Cowley et al. 2010), HD 104237 (da Silva et al. 2009), HD 143006 (Jönsson et al. 2020), HD 169142 (Alecian et al. 2013), PX Vul (Pereyra et al. 2009) and BP Psc (Torres et al. 2006). Finally, the value of $v \sin i$ for BF Ori was directly adopted from Mora et al. (2001).

3.2. Surface gravities and metallicities

Figure 1 illustrates the steps followed in the estimation of $\log g$ and [M/H]. First, for each star, we generated an initial grid of Kurucz models, with the corresponding T_{eff} and $v \sin i$ listed in Tables A.1 and A.2, $\log g = 3.5$, 4.0, 4.5 and [M/H] $= -2.5, -2.0, -1.5, -1.0, -0.5, 0.0, +0.2$, and $+0.5$. From this point on, two different paths were followed depending on the T_{eff} of the source.

For stars with $T_{\text{eff}} > 8000$ K, $\log g$ was derived by comparing the observed widths of the Balmer lines Hδ, Hγ, and Hβ at intensity 0.80 with those from the models (Gray & Corbally 2009). The initial grid was interpolated in order to obtain the $\log g$ values that provide the best fit for each line, the final value being the average of the previous. Uncertainties were calculated from the standard deviation of the individual $\log g$ values obtained in each of the considered Balmer lines. Lines affected by strong emission components that do not allow for the wings of the absorption profiles to be correctly traced were excluded from the analysis (see the example in the top-right panel of Fig. 2).

Once the value of $\log g$ was determined, the observed and modeled pseudo-equivalent widths (pEW) were compared to each other for the different [M/H] values, providing a final value of [M/H] based on a χ^2 test. A pEW is defined exactly in the same way as the classical EW, but instead of characterizing a single spectral line, the measurement extends over several lines within a wavelength range $[\lambda_1, \lambda_2]$. The reason for using pEW instead of EW is that the former is less limited by spectral resolution. Indeed, most stars in the sample show large values of $v \sin i$, which makes an individual analysis of the spectral lines difficult due to blending. Moreover, the lower spectral resolution of the X-shooter spectra, which are intensively used, prevents us from measuring EWs of individual lines accurately, even in objects with moderately small values of $v \sin i$. A similar method to estimate metallicities was developed by Gray et al. (2002) but in a different context (i.e., G and K giants; see, e.g., Lillo-Box et al. 2014, for a practical application of that formalism).

The wavelength region used to calculate the pEWs is [5000, 7000] Å. The windows initially selected were 80-Å wide, excluding the broad interval containing Hα, and the number of such windows per object was about six. However, for each source, a careful selection of what intervals within these windows were usable was carried out. Several factors prevented us from selecting the same regions homogeneously for all the stars, namely: (i) the presence of emission lines; (ii) the normalization of particular sections of the stellar spectrum; (iii) a low S/N, which causes some lines not to be discernible and difficulties to trace the continuum; (iv) scarcity of spectral lines (especially in very hot stars); (v) circumstellar contribution in absorption, superimposed to the photospheric lines; and (vi) variability. Regarding
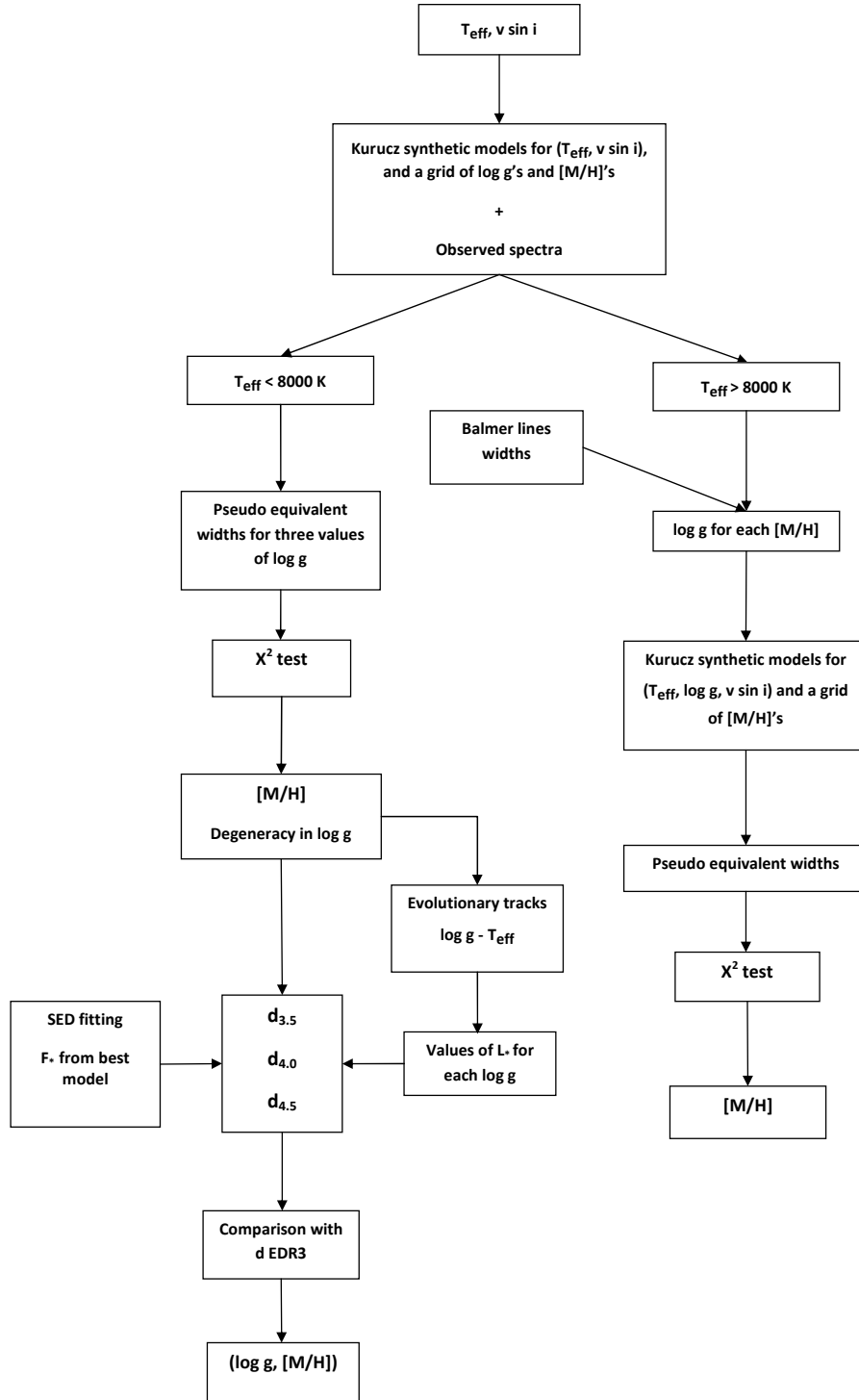
Fig. 1. Flow chart summarizing the process followed in the estimation of the $\log g$ and [M/H] values (see Sect. 3).

the last point, when multi-epoch spectra are available for a given source, they were checked to avoid regions where variability in the profiles of the metallic lines was apparent. It should also be mentioned that some spectra had to be renormalized manually in order to obtain a better estimate of [M/H].

As a reference for the final [M/H] value, we used that given by the χ^2 test, while the corresponding uncertainty was estimated from the individual [M/H] best-fitting value of each spectral region considered. An average of the absolute errors was computed, assuming a minimum uncertainty of 0.10 dex.

A different procedure was followed for stars with $T_{\rm eff} \leq$ 8000 K. The widths of the Balmer lines are insensitive to changes in surface gravity for such sources (Gray & Corbally 2009); spectral indicators for this kind of objects based on lines ratios are difficult to apply, given their typically large values of $v \sin i$. Therefore, in these cases moved directly to the step where the pEWs are calculated in the observed spectrum and in the whole collection of models (Fig. 1). Hence, the result of the χ^2 test yields a value of [M/H], but with a degeneracy in $\log g$. In fact, the three best models with $\log g = 3.5, 4.0, 4.5$ fit the regions of
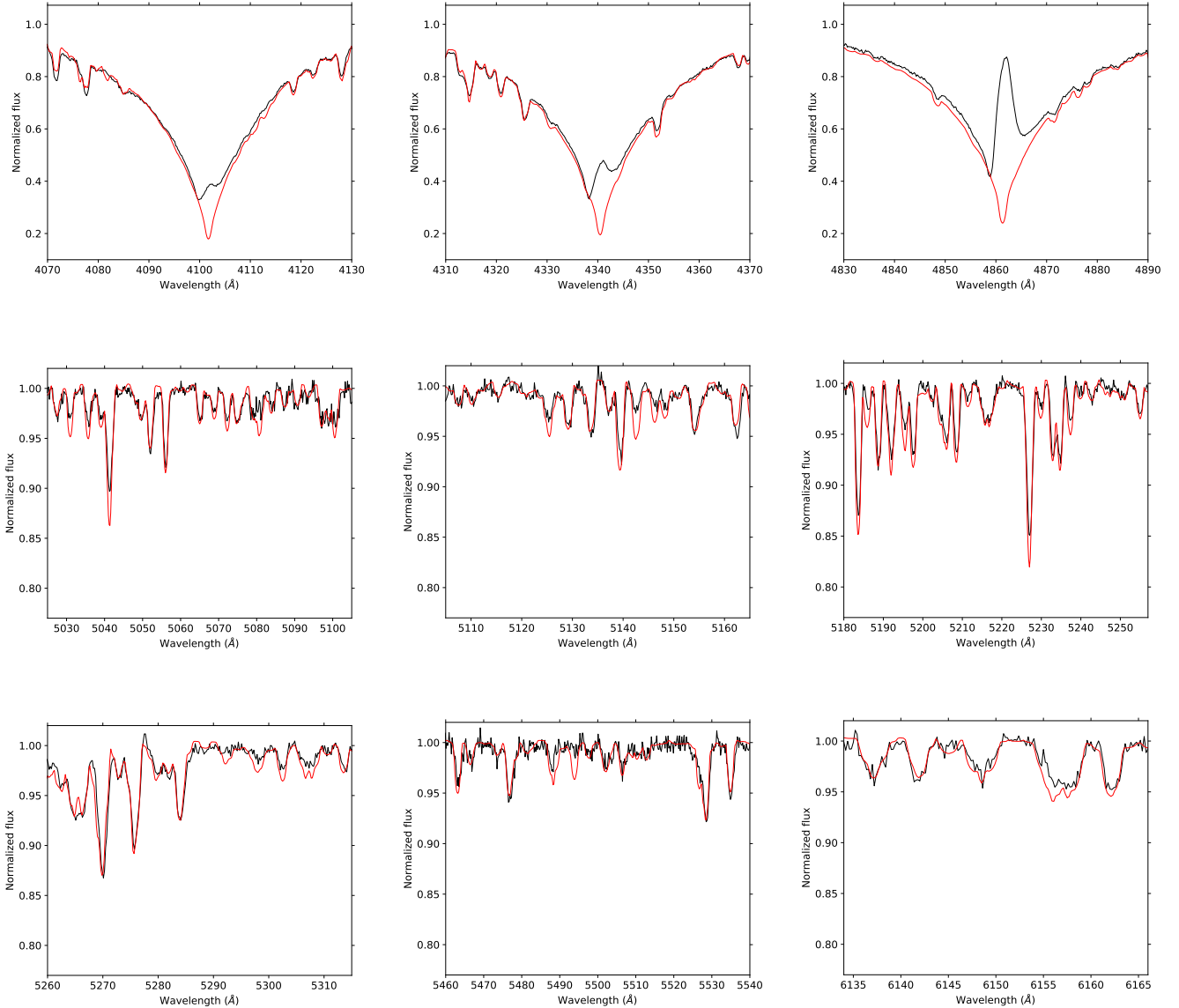
Fig. 2. Fits of the Balmer lines Hδ, Hγ, Hβ, and six regions of the HD 244314 spectrum (black solid line) with the best model obtained in the χ^2 test (red solid line). The model has been generated with a $T_{\rm eff}$ = 8500 K, $\log g$ = 4.08, $v \sin i$ = 55 km s^{-1} and [M/H] = 0.0. In this example, the line Hβ has not been considered in the estimation of $\log g$ as it shows a strong emission.

the observed spectrum practically in the same way, hardly showing any variation in the pEWs of the regions explored. In order to find out which $\log g$ is closer to the stellar value, we have used an indirect method that consists of determining which of these $\log g$ is consistent with the distance from *Gaia* (E)DR3 (Lindegren et al. 2021; Gaia Collaboration 2023, see also Table B.1 of Guzmán-Díaz et al. 2021).

Let us denote d$_{3.5}$, d$_{4.0}$, and d$_{4.5}$, the distances implied from the three values of $\log g$. These distances are derived from the expression $d = \sqrt{L_*/4\pi F_*}$, where L_* is the stellar luminosity, and F_* is the total observed flux from the star. The fluxes were calculated using the VOSA[4] tool by integrating the -dereddened-Kurucz ODFNEW/NOVER models (Castelli et al. 1997) computed for $T_{\rm eff}$, [M/H] from the χ^2 test, and the three values of $\log g$. Although the visual extinction (A_v) was left virtually free in the fits, their final values obtained for each log g are similar to those shown in Table B.1 of Guzmán-Díaz et al. (2021). The

stellar luminosities were derived by translating the points ($T_{\rm eff}$, $\log g$; with $\log g$ = 3.5, 4.0, 4.5) from the $T_{\rm eff}$ - $\log g$ HR diagram to the $T_{\rm eff}$ - $\log L_*$ diagram. PARSEC V2.1s[5] evolutionary tracks (Bressan et al. 2012) were used. Each one of the three points ($T_{\rm eff}$, $\log g$) has a one-to-one corresponding point ($T_{\rm eff}$, $\log L_*$); once d$_{3.5}$, d$_{4.0}$ and d$_{4.5}$ are computed, the stellar gravity is the one whose derived distance matches that from *Gaia* (E)DR3. Interpolation between distances was used when required. A typical error of 0.05 dex on $\log g$ was adopted.

In some stars, two different values of [M/H] provide similar values of χ^2. For these cases, we generated new models by interpolating the values of [M/H] and repeated the χ^2 test in order to check if a better fit was obtained. Should this occur, we assumed this new value; otherwise, the [M/H] with the lowest χ^2 retrieved from the previous test was kept.

Table A.2 lists the final values inferred for $\log g$ and [M/H] and their corresponding errors in Cols. 5 and 6. Figure 2 shows
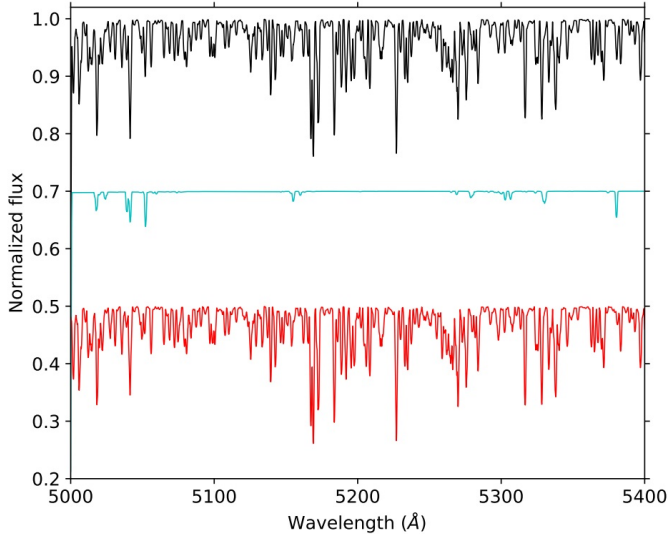

Fig. 3. Model with T_{eff} = 8000 K, $v \sin i$ = 50 km s^{-1}, and [M/H] = 0.0 in the 5000–5400 Å region is represented in black, while only the C, O, and S lines generated with the same parameters are shown in cyan. The result of subtracting the volatile elements from the first model is shown in red. The models were shifted on the y-axis for clarity.

a representative example of the best fit obtained applying the procedure described above for HD 244314.

3.3. Interpretation of the [M/H] derived in this work

In order to interpret the results, it is important to emphasize explicitly that the method used does not take into account variations of individual abundances of specific elements, that is, for a given [M/H], all abundances are scaled in the same manner to the solar one by a factor $10^{[M/H]}$, the whole procedure providing an average metal abundance for each star.

Since the hypothesis by Kama et al. (2015) linked a deficit of refractory elements to the presence of dust traps and cavities potentially caused by Jovian planets, we carried out the following exercise: all lines of C, O, N, and S in the interval 5000–7000 Å were identified and the pEWs were computed in the same regions both in the stellar spectra and in the models, avoiding the small windows where lines of those volatile elements appear. Given that the number of lines of volatiles is much less than that of refractories, it turned out that the new [M/H] values do not show significant changes when compared with the initial calculations.

The previous test was done for six stars of the sample with different values of T_{eff}, $v \sin i$, and [M/H] to cover a representative set of parameters, finding no significant differences with respect to the values already listed in Table A.2. Figure 3 shows an example of how the subtraction of the C, O, N, and S lines from a synthetic model hardly produces any change in the 5000–5400 Å region, which serves to visualize why the [M/H] measurements are mainly determined by the abundances of refractory elements regardless of the abundances of volatiles.

4. Analysis and discussion

4.1. Consistency tests

4.1.1. Comparison with previous results

The top panel of Fig. 4 compares the values estimated here for $v \sin i$ with previous values from the literature, which are
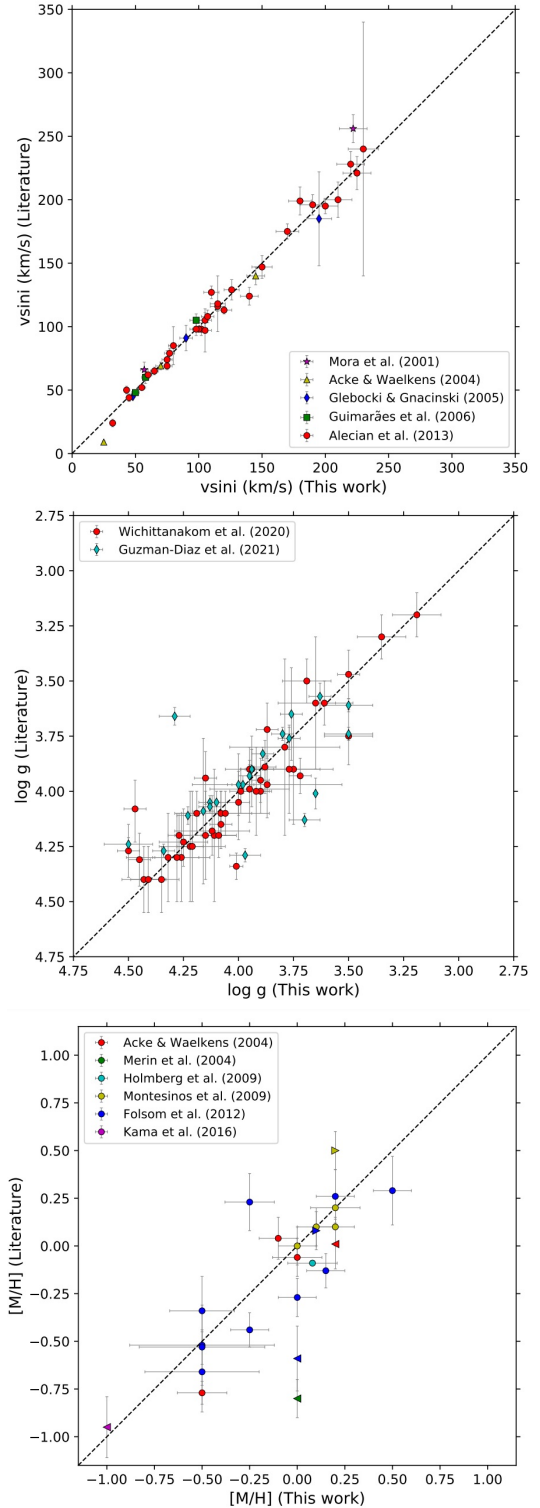
Fig. 4. $v \sin i$, $\log g$ and [M/H] are compared with the values found in the literature (as indicated in the legends). Error bars represent the uncertainties in these parameters, while the lower and upper limits are denoted by right- and left-pointing triangles, respectively. The black dashed line indicates equal values.

available for 63% of the stars in our sample. For those values in the literature where no associated error was found, an uncertainty of 5% was assumed. Results are in good agreement for the majority of the stars, being the mean relative error ~7%. The previous analysis excludes the ten stars (shown in Table A.2)

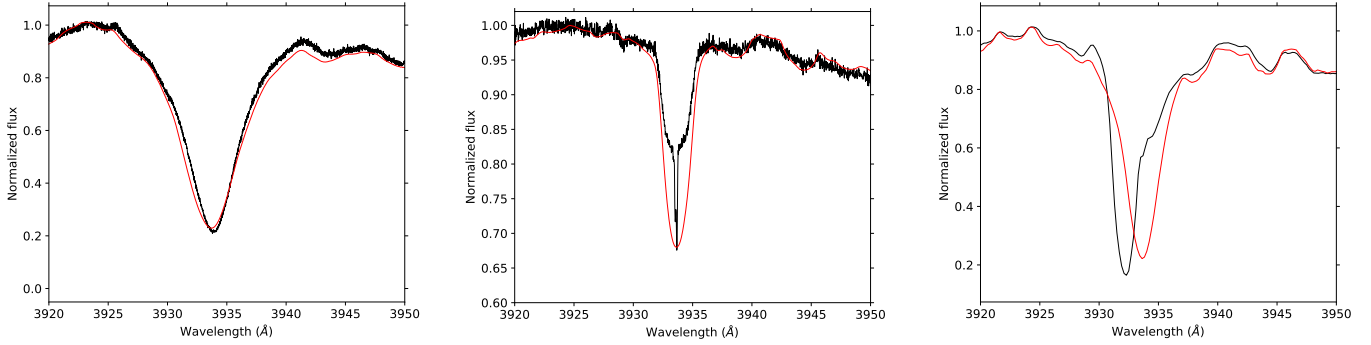**Fig. 5.** Ca II K lines of the spectra of the stars (black solid lines) HD 39014 (*left*), HD 132947 (*middle*), and HD 31648 (*right*), and the corresponding best-fitting models (red solid lines). A good fit is only achieved in the first case, where no circumstellar contribution or peculiar profiles are apparent.

with $v \sin i$ values based or directly adopted from the literature (Sect. 3.1).

Concerning $\log g$, our values and previous ones based on the literature are plotted against each other in the middle panel of Fig. 4. In this case, the comparison has been possible for the whole sample; the $\log g$ values not available in Wichittanakom et al. (2020) have been computed from the expression $g = GM_*/R_*^2$, taking the stellar mass, M_*, and radius, R_*, from Guzmán-Díaz et al. (2021). The corresponding uncertainties have been calculated by error propagation. The absolute error for most objects is below 0.20 dex, with 18% of them showing an error larger than that value.

Finally, the comparison between the [M/H] values from this work and from the literature is included in the bottom panel of Fig. 4, which was feasible for 36% of the stars in the sample. Literature values come from Montesinos et al. (2009) and Kama et al. (2015). In turn, Kama et al. (2015) compiled individual abundances of certain elements from Acke & Waelkens (2004) and Folsom et al. (2012), except for HD 34282 (Merín et al. 2004), HD 100546 (Kama et al. 2016), and HD 142527 (Holmberg et al. 2009). In order to convert such abundances into metallicitiy values, we followed the process described in the appendix of Montesinos et al. (2009), considering only the abundances of Fe, Si, and Mg given in Kama et al. (2015). There is a reasonable agreement between our results and those from the literature, and the sources identified as having low- and high-[M/H] coincide. The mean absolute difference is approximately ±0.15 dex, excluding the sources with lower and upper limits. Notes on specific sources where the differences between our [M/H] values and those from the literature are relevant are presented in Appendix B.

4.1.2. The Ca II K line

The depth of the Ca II K line is used in main sequence A-type stars as the prime estimator of their effective temperature (Gray & Corbally 2009). However, following other works devoted to the determination of stellar parameters of HAeBes (e.g., Acke & Waelkens 2004; Folsom et al. 2012), this line has also been excluded from the whole procedure devised in this work. The reason is that most stars in the sample show Ca II K lines with circumstellar contributions and/or peculiar profiles that pure photospheric models are not able to reproduce. In addition, the blue part of the spectrum would be affected by veiling in those cases where the accretion contribution to the total flux starts to be comparable to the photospheric flux.

With the previous caveat in mind, we checked how the best-fitting models from the χ^2 tests match the observed Ca II K
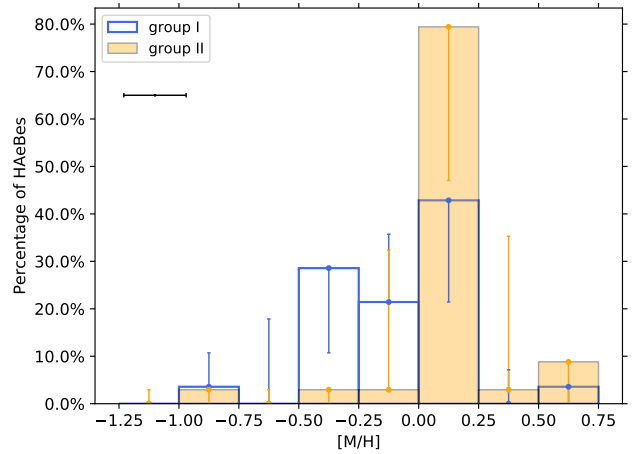

Fig. 6. Histograms comparing the distributions of metallicities and SED classification, as indicated in the *x*-axis and the legend. Vertical error bars represent the variations of the number of stars contained in each bin considering the individual uncertainties in [M/H], whose typical value is represented by the horizontal error bar below the legend.

profile for stars with $T_{\rm eff}$ between 8000 K and 10 500 K (A5 - B9). For the few stars with normal, symmetric profiles, the models reproduce the line profile with a reasonable level of accuracy, which constitutes an additional proof of self-consistency. Figure 5 shows three representative examples. For HD 39014 the model fits the Ca II K line reasonably well, HD 132947 shows a circumstellar component superimposed to the photospheric profile, and, finally, HD 31648. presents a peculiar profile that the model is unable to reproduce.

4.2. [M/H] and SED groups

Figure 6 shows the [M/H] distribution of the sample analyzed, where the blue and orange histograms refer to group I and group II sources, respectively. Although most HAeBes tend to show [M/H] values close to solar, the relative fraction of group I sources having sub-solar values is larger (~55%) than that for group II (~10%). In particular, the median [M/H] is −0.10 for group I and +0.14 for group II HAeBes. We carried out a Kolmogorov-Smirnov (KS) test to verify whether the group I and group II HAeBes have different [M/H] distributions or not. The result obtained is that there is a negligible probability (p-value = 0.003) that both samples are drawn from the same parent distribution at a 1% significant level. An Anderson-Darling (AD) test, more sensitive to the tails of the distributions than the
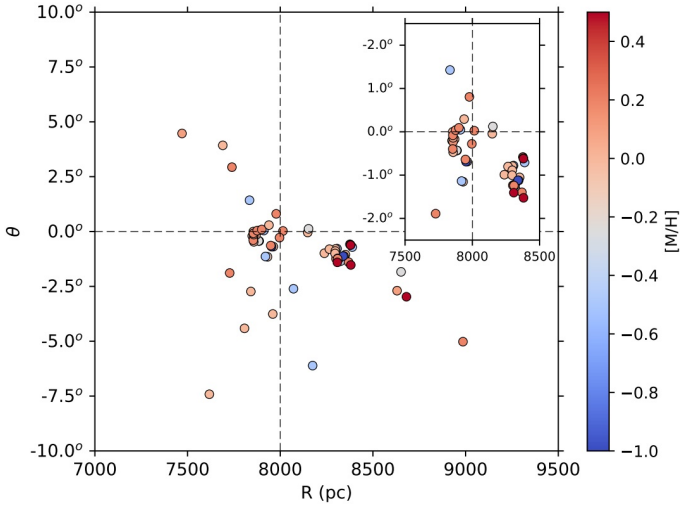
Fig. 7. 2D representation of the distribution in the Galaxy of the HAeBes studied in this work. The Galactic azimuthal angle in the *y*-axis is plotted against the distance to the Galactic center in the *x*-axis. The colour bar indicates their [M/H] values. The most crowded region of the plot has been zoomed in. The values for the sun – with [M/H] = 0 – are also indicated with the vertical and horizontal dashed lines, for reference.

KS test, also rejects the null hypothesis that both group I and group II samples are drawn from the same parent distribution at the same significance level. Whether the upper and lower limits in the histograms are considered or not does not significantly alter the results provided by the KS and AD tests.

In short, our enlarged sample of HAeBes, with the homogeneously derived [M/H] values and SED classification according to the Meeus et al. (2001) scheme, statistically confirms the finding by Kama et al. (2015). Specifically, group I and group II sources tend to show different distributions of [M/H] values, with group I sources being less metallic than group II.

4.3. A possible link with planet formation

In the following sections, we aim to interpret the previous observational trend linking low stellar metallicities with group I sources, focusing on the plausibility of the scenario in which giant planets trapping refractory elements are more frequent around HAeBes with such a type of SED (Kama et al. 2015).

4.3.1. Galactic distribution of group I and group II HAeBes

The first question to be addressed is whether different stellar metallicities are actually associated with different SED groups or whether these could instead be driven by environmental effects. Given that the mixing timescale for radiative sub-photospheric regions such as those of HAeBes is similar to their typical ages (~Myr), the second possibility cannot be neglected. For instance, we may wonder if the low- and high-[M/H] stars are located in different clusters or regions within the Galaxy, in which case the stellar metallicities may reflect the local, initial conditions. However, no significant difference is found concerning the clustering properties of the low- and high-[M/H] stars in our sample, which appear mixed together and sharing common regions (Fig. 7). A similar result is obtained for the whole sample classified by Guzmán-Díaz et al. (2021) in 112 group I and 70 group II HAeBes.
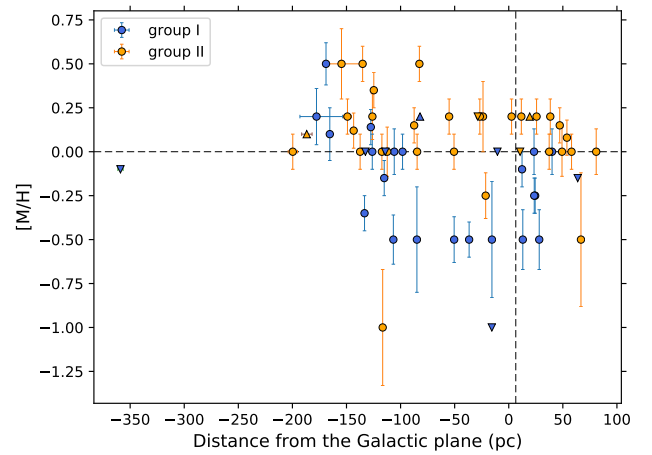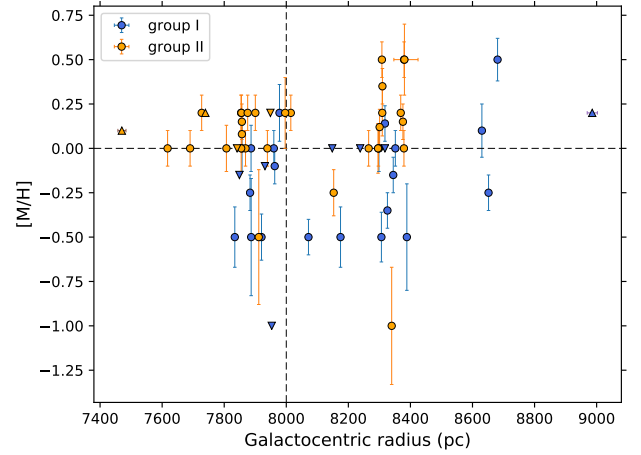
Fig. 8. Metallicity of the stars in our sample versus the distance to the Galactic center (*top*) and to the galactic plane (*bottom*). Group I and II sources are color coded as indicated in the legends. The lower and upper limits are indicated by the up and down triangles. The values of the sun are also indicated with the vertical and horizontal dashed lines, for reference.

We also tested whether the trend linking lower metallicities to group I sources could be related to the well-known empirical relations showing that stellar abundances depend on both the distance to the Galactic center and to the Galactic plane (e.g., Adibekyan et al. 2014; Hawkins 2022, and references therein). The top and bottom panels of Fig. 8 show the [M/H] estimated in this work versus the galactocentric radius and the vertical distance to the galactic plane, respectively. The scatter observed in both panels indicates that the observed differences between the typical metallicities of group I and group II sources are not driven by [M/H] gradients on a Galactic scale, at least for the HAeBes analyzed here. We can therefore conclude that the [M/H] values of the stars in our sample do not depend on where they were born, retaining the hypothesis from Kama et al. (2015) as a possible cause for the different metallicities between group I and group II HAeBes.

4.3.2. [M/H] and transitional disks

The last column of Table A.1 lists the type of SED shown by each star in the sample according to the "JHK classification" carried out in Guzmán-Díaz et al. (2021). According to this classification, stars are divided in four groups (J, H, Ks, and
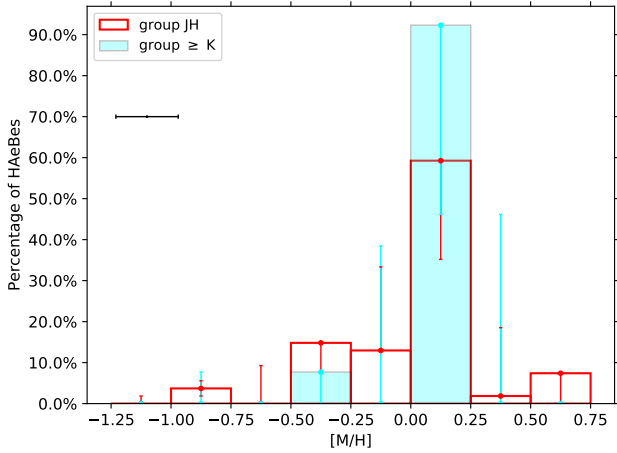
Fig. 9. Histograms comparing the distributions of metallicities and JHK classification, as indicated in the *x*-axis and the legend. Vertical error bars represent the variations of the number of stars contained in each bin considering the individual uncertainties in [M/H], whose typical value is represented by the horizontal error bar below the legend.
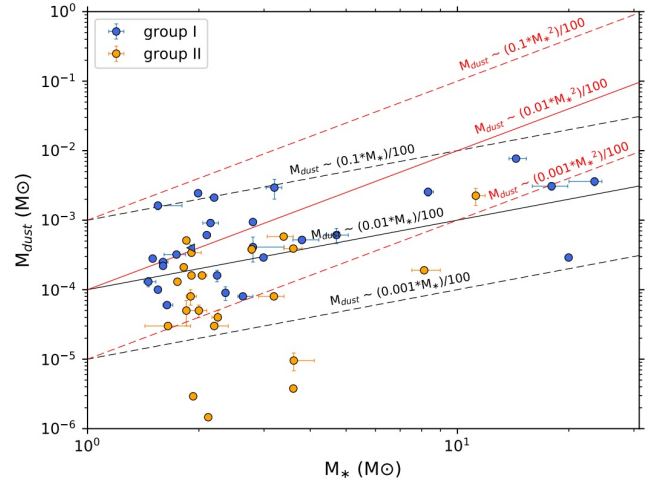

Fig. 10. Dust disk mass versus stellar mass for most HAeBes having (sub)mm emission, as compiled in Guzmán-Díaz et al. (2021). Group I and II sources are color coded as indicated in the legend. Typical power-law trends with exponents 1 and 2 are also shown in black and red, respectively. The corresponding ±1 dex scatter are indicated with dashed lines.

>Ks), indicating the shortest near-infrared band where excess emission over the photosphere is already present. As detailed in Guzmán-Díaz et al. (2021), and references therein, such a classification can be related to the size of the holes in the inner dust disks, being the Ks and >Ks sources associated with so-called "transitional disks" with relatively large inner holes.

Figure 9 shows the [M/H] distribution of the sample analyzed, where this time the red and cyan histograms refer to non-transitional and transitional disks as inferred from the JHK classification. Based on the KS and AD tests, the null hypothesis that both sub-samples are drawn from the same parent distribution cannot be rejected, contrasting with the analogous analysis in Sect. 4.2 concerning the SED groups.

The fact that [M/H] is not related to the presence of transitional disks (as inferred from SEDs) indicates that the stellar abundances are not generally affected by the different processes that may cause the appearance of dust inner holes. Such holes can be related to other mechanisms apart from the presence of planets, such as grain growth, dust settling, or photoevaporation (e.g., Espaillat et al. 2014, and references therein). Indeed, most transitional disks in HAeBes seem to be related with the latter process and the high stellar luminosities, being much more frequent for stars with the earliest spectral types (HBes) than for the rest (see the discussion in Guzmán-Díaz et al. 2021, and references therein). In contrast, the cavities associated with group I sources may be related to the potential presence of giant planets, which could cause the metal depletion of the central stars (Kama et al. 2015).

4.3.3. Dust disk masses of group I and group II HAeBes

The formation of giant planets requires a large enough mass reservoir in the circumstellar environment. In fact, models predict better chances to host giant planets for the sources having larger disk masses, M_{disk}, within a similar stellar mass range (e.g., Alexander & Armitage 2007; Andrews et al. 2013). Guzmán-Díaz et al. (2021) found that the stellar mass distributions of hundreds of group I and II HAeBes are similar, providing M_{disk} based on (sub)mm continuum emission for many of them. Figure 10 shows the stellar versus dust disk mass ($M_{dust} = M_{gas}/100 \simeq M_{disk}/100$) distribution for most of

such sources. The stars from the sample of Guzmán-Díaz et al. (2021) with upper and lower limits in the continuum fluxes were discarded. The ones having excessive continuum emission leading to $M_{dust} > 0.01$ $M_{\odot}$, probably due to contamination from the surroundings, were not included in the plot either. It is apparent from the 27 group I and 22 group II HAeBes plotted in Fig. 10 that although both groups span over the same stellar mass range, M_{dust} (and hence M_{disk}) for group I stars tend to be larger than those for group II. Indeed, the median M_{dust} for group I and II stars is $(4\pm3) \times 10^{-4}$ $M_{\odot}$ and $(1\pm0.9) \times 10^{-4}$ $M_{\odot}$, respectively, with the uncertainties indicating the median absolute deviations. Moreover, a non-negligible fraction close to 20% of group II sources fall below the rough disk mass-stellar mass correlation found for most lower-mass stars (black and red lines in Fig. 10; see e.g., Andrews et al. 2013; Testi et al. 2022, and references therein).

A similar result indicating smaller M_{dust} in group II HAeBes was recently obtained by Stapper et al. (2022) from ALMA data. In addition to this result, Stapper et al. (2022) put forward an alternative explanation. This is that group I and group II sources may have similar M_{dust}, but with different spatial dust grain distributions. In particular, they hypothesized that in group II sources most of the dust is concentrated in the inner, compact regions of the disks. As a consequence, such regions would be optically thick, trapping the radiation and leading to the inference of a lower M_{dust} than they would actually be subject to. In contrast, the inner parts of the disks around group I sources would be optically thin due to presence of a cavity, allowing the radiation to escape and yielding larger M_{dust} than those in group II. In turn, Stapper et al. (2022) argued that the different dust grain distributions may be associated with the presence of giant planets in the disks of group I sources. Therefore, regardless of the interpretation the typically stronger (sub-)mm continuum emission of group I stars can currently be understood in terms of a higher probability to host giant planets, compared to group II HAeBes.

4.3.4. Planet candidates, metallicities, and SED groups

The hypothesis that giant planets are more likely present in disks around group I sources with low stellar metallicities than in

the rest of the HAeBes can only be unambiguously tested once a statistically significant sample of such planets are detected. However, confirming potential detections of forming planets in protoplanetary disks is still a challenging task (e.g., Mendigutía et al. 2018) and has only been possible around the low-mass T Tauri star PDS 70 (Keppler et al. 2018; Haffert et al. 2019). In addition, a possible forming planet has been recently discovered around the HAeBe star AB Aur (Currie et al. 2022, see also Zhou et al. 2022). The properties of this system are fully consistent with the above hypothesis: AB Aur belongs to group I (Guzmán-Díaz et al. 2021) and we derive a relatively small [M/H] = −0.35 ± −0.25 (based on the individual abundances in Kama et al. 2015, and the procedure indicated in Sect. 4.1.1).

In the rest of this section, we aim to provide a rough quantification about the possible presence of giant planets in relation with the SED groups and the stellar metallicities, based on observed disk structures from high-resolution techniques. It must be noted that such a quantification is difficult to assess, given that most (if not all) structures observed in protoplanetary disks can be potentially explained either invoking the presence of planets or different phenomena (for a recent example, see, e.g., Demidova & Grinin 2022).

An important exception may be the "velocity kinks", that is, perturbations of the Keplerian orbits of the gas, most probably caused by the presence of giant planets (Pinte et al. 2018; Teague et al. 2018, but see also Norfolk et al. 2022). Using such a technique Pinte et al. (2020) reported two HAeBes with plausible planets in their disks: HD 143006 and HD 163296. The previous sample can be complemented by the one in Asensio-Torres et al. (2021), where the most promising candidate young stars hosting planets based on SPHERE data were analyzed. In that work, the masses of possible giant planets capable of generating the structures observed in scattered light (rings, cavities, spirals) were estimated for the HAeBes HD 100546, HD 135344B, HD 139614, HD 97048, HD 169142, CQ Tau, HD 34282, and HD 36112.

One of the most striking features when grouping together the HAeBes of both previous works (plus AB Aur, making a total of 11 stars) is that all sources, except HD 163296, are classified as group I (Guzmán-Díaz et al. 2021). Considering the previous numbers alone, the probability of detecting disks with substructures presumably related to the presence of giant planets is about ten times larger in group I sources than in group II stars. However, the previous estimate must be considered as an upper limit, given that high-resolution observations are still biased towards brighter and more extended group I sources (Garufi et al. 2018, 2022). Concerning [M/H], none of the mentioned stars exceed the solar one except HD 163296 with [M/H] ∼ 0.2 (Table A.2) and HD 36112 with [M/H] ∼ 0.09 (as inferred from the values in Kama et al. 2015, and the procedure of Sect. 4.1.1). The crude estimate presented above suggests that current high-resolution data indeed support that group I sources with relatively small values of [M/H] are better candidates to host giant planets than the rest of the HAeBes.

5. Conclusions and final remarks

In this work, we derive estimates of [M/H] for 67 HAeBe stars. This is, to our knowledge, the largest sample of such objects for which these values have been derived homogeneously, complementing our previous work on the stellar and circumstellar properties of HAeBes. Values of $\log g$ and $v \sin i$ are additional byproducts of the analysis. Our new data have served to robustly confirm the proposal presented by Kama et al. (2015), namely,

that HAeBes with group I SEDs typically show lower [M/H] values than those of group II. The hypothesis put forward by Kama et al. (2015) to explain this observational fact is that the presence of dust traps and cavities, potentially caused by Jovian planets trapping the refractory elements, are more frequent in disks of group I HAeBes. We provide further evidence that reinforces this hypothesis:

– The [M/H] values of the HAeBes in our sample and the distinctions between group I and II sources do not depend on their location within the galaxy, suggesting that the observed differences in [M/H] are not caused by the local environment but are most likely connected with the cavities associated with group I stars. In contrast, we do not find any relation between [M/H] and SED-based transitional disks without infrared excess at least up to ∼2.2 μm, indicating that not all mechanisms causing the associated holes (such as photoevaporation) affect the abundances of the central stars.

– We confirm that the (sub-) mm continuum emission of group I stars is typically larger than that of group II. Regardless of the interpretation in terms of larger disk masses or different dust grain distributions, the previous finding is in line with the hypothesis that group I/low [M/H] sources are better candidates for hosting giant planets than the rest of the HAeBes.

– Current high-resolution imaging data available from the literature support the hypothesis as well, with the most promising giant planet-hosting candidates being mainly group I sources with relatively low metallicities.

We note that our results do not rule out the presence of giant planets in disks around group II, high-metallicity sources. Strictly speaking, our results suggest that giant planets may trap the refractory material more frequently in group I sources than in group II, at least during the evolutionary stage represented by each group. Nevertheless, exoplanet synthesis models indicate that while the effect of metallicity in forming planets is relevant for low-mass stars, giant planet formation can occur in a low-metallicity (low dust-to-gas ratio) and high-mass protoplanetary disks surrounding higher mass sources (Alibert et al. 2011). Indeed, Maldonado & Villaver (2016) reported that giant stars with planets do not show the metal-rich signature. This fact could be explained by the more massive protoplanetary disks of their progenitors, since these sources are more massive than the typical FGK stars that are the main focus of the planet searches around main sequence stars.

An unambiguous confirmation of the relation between group I/low [M/H] HAeBes and the presence of giant planets in the process of formation would represent a major step towards our understanding about planet frequencies around A an B stars, bridging the gap with the FGK stars mainly explored by exoplanet surveys. The current situation is ideal for that purpose, with hundreds of HAeBes recently identified and thousands of new potential members thanks to *Gaia* data. However, such a confirmation requires the actual detection of forming planets around HAeBes, which is currently limited to the candidate around the group I/ low [M/H] star AB Aur.

References

Acke, B., & Waelkens, C. 2004, A&A, 427, 1009
Adibekyan, V. 2019, Geosciences, 9, 105
Adibekyan, V. Z., González Hernández, J. I., Delgado Mena, E., et al. 2014, A&A, 564, L15
Alecian, E., Wade, G. A., Catala, C., et al. 2013, MNRAS, 429, 1001
Alexander, R. D., & Armitage, P. J. 2007, MNRAS, 375, 500
Alibert, Y., Mordasini, C., & Benz, W. 2011, A&A, 526, A63
Andrews, S. M., Rosenfeld, K. A., Kraus, A. L., & Wilner, D. J. 2013, ApJ, 771, 129
Arun, R., Mathew, B., Manoj, P., et al. 2019, AJ, 157, 159
Asensio-Torres, R., Henning, T., Cantalloube, F., et al. 2021, A&A, 652, A101
Booth, R. A., & Owen, J. E. 2020, MNRAS, 493, 5079
Bressan, A., Marigo, P., Girardi, L., et al. 2012, MNRAS, 427, 127
Castelli, F., & Kurucz, R. L. 2003, IAU Symp., 210, A20
Castelli, F., Gratton, R. G., & Kurucz, R. L. 1997, A&A, 318, 841
Cowley, C. R., Hubrig, S., González, J. F., & Savanov, I. 2010, A&A, 523, A65
Cretignier, M., Francfort, J., Dumusque, X., Allart, R., & Pepe, F. 2021, Astrophysics Source Code Library [record ascl:2102.022]
Currie, T., Lawson, K., Schneider, G., et al. 2022, Nat. Astron., 6, 751
da Silva, L., Torres, C. A. O., de La Reza, R., et al. 2009, A&A, 508, 833
Demidova, T. V., & Grinin, V. P. 2022, ApJ, 930, 111
Dullemond, C. P. 2002, A&A, 395, 853
Dullemond, C. P., & Dominik, C. 2004, A&A, 417, 159
Espaillat, C., Muzerolle, J., Najita, J., et al. 2014, in Protostars and Planets VI, eds. H. Beuther, R. S. Klessen, C. P. Dullemond, & T. Henning (Tucson: University of Arizona Press), 497
Folsom, C. P., Bagnulo, S., Wade, G. A., et al. 2012, MNRAS, 422, 2072
Gaia Collaboration (Vallenari, A., et al.) 2023, A&A, in press https://doi.org/10.1051/0004-6361/202243940
Garufi, A., Meeus, G., Benisty, M., et al. 2017, A&A, 603, A21
Garufi, A., Benisty, M., Pinilla, P., et al. 2018, A&A, 620, A94
Garufi, A., Dominik, C., Ginski, C., et al. 2022, A&A, 658, A137
Glebocki, R., & Gnacinski, P. 2005, VizieR Online Data Catalog: III/244
Gonzalez, G. 1997, MNRAS, 285, 403
Gray, D. F., Scott, H. R., & Postma, J. E. 2002, PASP, 114, 536
Gray, R. O., & Corbally, C. J. 1998, AJ, 116, 2530
Gray, R. O., & Corbally, Christopher, J. 2009, Stellar Spectral Classification (Princeton: Princeton University Press)
Guimarães, M. M., Alencar, S. H. P., Corradi, W. J. B., & Vieira, S. L. A. 2006, A&A, 457, 581
Guzmán-Díaz, J., Mendigutía, I., Montesinos, B., et al. 2021, A&A, 650, A182
Haffert, S. Y., Bohn, A. J., de Boer, J., et al. 2019, Nat. Astron., 3, 749
Hawkins, K. 2022, MNRAS, submitted [arXiv:2207.04542]
Herbig, G. H., & Bell, K. R. 1988, Third Catalog of Emission-Line Stars of the Orion Population : 3 : 1988 (Santa Cruz: Lick Observatory)

Holmberg, J., Nordström, B., & Andersen, J. 2009, A&A, 501, 941
Honda, M., Maaskant, K., Okamoto, Y. K., et al. 2015, ApJ, 804, 143
Jermyn, A. S., & Kama, M. 2018, MNRAS, 476, 4418
Jönsson, H., Holtzman, J. A., Allende Prieto, C., et al. 2020, AJ, 160, 120
Kama, M., Folsom, C. P., & Pinilla, P. 2015, A&A, 582, L10
Kama, M., Bruderer, S., van Dishoeck, E. F., et al. 2016, A&A, 592, A83
Keppler, M., Benisty, M., Müller, A., et al. 2018, A&A, 617, A44
Kluska, J., Van Winckel, H., Coppée, Q., et al. 2022, A&A, 658, A36
Kuhn, M. A., Saber, R., Povich, M. S., et al. 2023, AJ, 165, 3
Lillo-Box, J., Barrado, D., Moya, A., et al. 2014, A&A, 562, A109
Lindegren, L., Klioner, S. A., Hernández, J., et al. 2021, A&A, 649, A2
Maaskant, K. M., Honda, M., Waters, L. B. F. M., et al. 2013, A&A, 555, A64
Maldonado, J., & Villaver, E. 2016, A&A, 588, A98
Maldonado, J., Eiroa, C., Villaver, E., Montesinos, B., & Mora, A. 2012, A&A, 541, A40
Maldonado, J., Eiroa, C., Villaver, E., Montesinos, B., & Mora, A. 2015, A&A, 579, A20
McGinnis, P., Dougados, C., Alencar, S. H. P., Bouvier, J., & Cabrit, S. 2018, A&A, 620, A87
Meeus, G., Waters, L. B. F. M., Bouwman, J., et al. 2001, A&A, 365, 476
Mendigutía, I., Calvet, N., Montesinos, B., et al. 2011, A&A, 535, A99
Mendigutía, I., Fairlamb, J., Montesinos, B., et al. 2014, ApJ, 790, 21
Mendigutía, I., Oudmaijer, R. D., Schneider, P. C., et al. 2018, A&A, 618, L9
Merín, B., Montesinos, B., Eiroa, C., et al. 2004, A&A, 419, 301
Montesinos, B., Eiroa, C., Mora, A., & Merín, B. 2009, A&A, 495, 901
Mora, A., Merín, B., Solano, E., et al. 2001, A&A, 378, 116
Muzerolle, J., D'Alessio, P., Calvet, N., & Hartmann, L. 2004, ApJ, 617, 406
Norfolk, B. J., Pinte, C., Calcino, J., et al. 2022, ApJ, 936, L4
Oomen, G.-M., Van Winckel, H., Pols, O., & Nelemans, G. 2019, A&A, 629, A49
Osborn, A., & Bayliss, D. 2020, MNRAS, 491, 4481
Pereyra, A., Magalhães, A. M., & de Araújo, F. X. 2009, A&A, 495, 195
Pinte, C., Price, D. J., Ménard, F., et al. 2018, ApJ, 860, L13
Pinte, C., Price, D. J., Ménard, F., et al. 2020, ApJ, 890, L9
Santos, N. C., Israelian, G., & Mayor, M. 2000, A&A, 363, 228
Santos, N. C., Israelian, G., & Mayor, M. 2001, ArXiv e-prints [arXiv:astro-ph/0109018]
Stapper, L. M., Hogerheijde, M. R., van Dishoeck, E. F., & Mentel, R. 2022, A&A, 658, A112
Teague, R., Bae, J., Bergin, E. A., Birnstiel, T., & Foreman-Mackey, D. 2018, ApJ, 860, L12
Testi, L., Natta, A., Manara, C. F., et al. 2022, A&A, 663, A98
Torres, C. A. O., Quast, G. R., da Silva, L., et al. 2006, A&A, 460, 695
Vioque, M., Oudmaijer, R. D., Baines, D., Mendigutía, I., & Pérez-Martínez, R. 2018, A&A, 620, A128
Vioque, M., Oudmaijer, R. D., Schreiner, M., et al. 2020, A&A, 638, A21
Vioque, M., Oudmaijer, R. D., Wichittanakom, C., et al. 2022, ApJ, 930, 39
Wichittanakom, C., Oudmaijer, R. D., Fairlamb, J. R., et al. 2020, MNRAS, 493, 234
Zhang, Y.-J., Hou, W., Luo, A. L., et al. 2022, ApJS, 259, 38
Zhou, Y., Sanghi, A., Bowler, B. P., et al. 2022, ApJ, 934, L13

Appendix A: Tables

Table A.1: Sample and properties

Object	RA (h:m:s)	DEC (d:m:s)	T_{eff} (K)	$\text{Log}(L_*)$ ($L_\odot$)	M_* ($M_\odot$)	Age (Myr)	Meeus group	JHK group
PDS 2	01 17 43.5	-52 33 31	6750±125	$0.77^{+0.01}_{-0.01}$	$1.46^{+0.04}_{-0.01}$	$15.04^{+2.67}_{-2.50}$	I	J
HD 9672	01 34 37.9	-15 40 35	9000±125	$1.20^{+0.02}_{-0.02}$	$1.93^{+0.02}_{-0.03}$	$11.02^{+8.96}_{-1.15}$	II	> Ks
HD 31648	04 58 46.3	+29 50 37	8000±125	$1.22^{+0.01}_{-0.01}$	$1.85^{+0.04}_{-0.01}$	$7.71^{+0.23}_{-0.38}$	II	J
UX Ori	05 04 30.0	-03 47 14	8500±250	$1.12^{+0.14}_{-0.20}$	$1.91^{+0.04}_{-0.00}$	$9.84^{+0.17}_{-0.00}$	II	J
HD 34282	05 16 00.5	-09 48 35	9500±250	$1.16^{+0.02}_{-0.02}$	< 1.90	< 19.87	I	J
HD 290380	05 23 31.0	-01 04 24	6250±125	$0.81^{+0.01}_{-0.01}$	$1.59^{+0.06}_{-0.06}$	$9.32^{+0.75}_{-1.31}$	II	J
HD 287823	05 24 08.0	+02 27 47	8375±125	$1.08^{+0.01}_{-0.01}$	$1.83^{+0.04}_{-0.03}$	$10.56^{+3.36}_{-0.62}$	I	J
V346 Ori	05 24 42.8	+01 43 48	7750±250	$0.86^{+0.01}_{-0.01}$	$1.65^{+0.04}_{-0.04}$	$16.21^{+3.37}_{-5.51}$	I	H
CO Ori	05 27 38.3	+11 25 39	6500±215	$1.36^{+0.12}_{-0.17}$	$2.30^{+0.06}_{-0.35}$	$3.92^{+2.07}_{-1.19}$	II	J
HD 35929	05 27 42.8	-08 19 39	7000±250	$1.97^{+0.02}_{-0.02}$	$3.53^{+0.08}_{-0.13}$	$1.20^{+0.30}_{-0.16}$	II	Ks
HD 290500	05 29 48.1	-00 23 43	9500±500	$1.10^{+0.06}_{-0.07}$	$1.85^{+0.05}_{-0.00}$	< 19.92	I	H
HD 244314	05 30 19.0	+11 20 20	8500±250	$1.29^{+0.02}_{-0.02}$	$2.12^{+0.04}_{-0.07}$	$6.99^{+0.63}_{-0.00}$	II	J
HD 244604	05 31 57.3	+11 17 41	9000±250	$1.53^{+0.02}_{-0.02}$	$2.16^{+0.04}_{-0.01}$	$5.08^{+0.16}_{-0.08}$	II	J
RY Ori	05 32 09.9	-02 49 47	6250±194	$0.80^{+0.09}_{-0.11}$	$1.58^{+0.17}_{-0.17}$	$9.42^{+2.19}_{-2.44}$	II	J
HD 36917	05 34 47.0	-05 34 15	11500±144	$2.61^{+0.03}_{-0.03}$	$4.36^{+0.08}_{-0.16}$	$0.89^{+0.09}_{-0.09}$	II	J
HD 245185	05 35 09.6	+10 01 51	10000±500	$1.48^{+0.02}_{-0.02}$	$2.24^{+0.05}_{-0.00}$	$7.08^{+0.06}_{-0.00}$	I	J
NV Ori	05 35 31.4	-05 33 09	7000±125	$1.33^{+0.03}_{-0.03}$	$2.09^{+0.06}_{-0.09}$	$5.04^{+0.85}_{-0.25}$	I	H
T Ori	05 35 50.5	-05 28 35	9000±500	$1.77^{+0.09}_{-0.12}$	$2.52^{+0.19}_{-0.21}$	$3.82^{+0.59}_{-0.82}$		J
CQ Tau	05 35 58.5	+24 44 54	6750±125	$0.82^{+0.01}_{-0.01}$	$1.50^{+0.01}_{-0.01}$	$12.42^{+2.40}_{-1.43}$	I	H
HD 37258	05 36 59.3	-06 09 16	9750±500	$1.41^{+0.02}_{-0.02}$	$2.27^{+0.03}_{-0.08}$	$5.94^{+1.01}_{-0.78}$	II	J
HD 290770	05 37 02.4	-01 37 21	10500±250	$1.74^{+0.01}_{-0.01}$	$2.64^{+0.13}_{-0.04}$	$4.01^{+0.39}_{-0.04}$	II	J
BF Ori	05 37 13.3	-06 35 01	9000±250	$1.13^{+0.09}_{-0.12}$	$1.85^{+0.15}_{-0.00}$	$17.14^{+2.80}_{-0.00}$	II	J
HD 37357	05 37 47.1	-06 42 30	9500±250	$1.94^{+0.08}_{-0.10}$	$2.80^{+0.20}_{-0.20}$	$2.96^{+0.44}_{-0.74}$	II	J
HD 290764	05 38 05.3	-01 15 22	7875±375	$1.34^{+0.02}_{-0.02}$	$1.99^{+0.03}_{-0.04}$	$6.10^{+0.62}_{-0.12}$	I	J
V599 Ori	05 38 58.6	-07 16 46	8000±250	$1.49^{+0.06}_{-0.07}$	$2.15^{+0.11}_{-0.10}$	$5.09^{+0.91}_{-0.51}$	I	J
V350 Ori	05 40 11.8	-09 42 11	9000±250	$0.96^{+0.21}_{-0.43}$	< 1.91	< 15.03	II	J
HD 38120	05 43 11.9	-04 59 50	11500±125	$1.85^{+0.02}_{-0.02}$	$2.80^{+0.04}_{-0.04}$	$3.95^{+0.08}_{-0.58}$	I	J
HD 39014	05 44 46.3	-65 44 08	8000±125	$1.66^{+0.01}_{-0.01}$	$2.48^{+0.07}_{-0.06}$	$3.52^{+0.28}_{-0.31}$	II	> Ks
PDS 124	06 06 58.5	-05 55 07	10250±250	$1.59^{+0.02}_{-0.02}$	$2.38^{+0.02}_{-0.05}$	$5.96^{+0.14}_{-0.75}$	I	H
LkHa 339	06 10 57.8	-06 14 40	10500±250	$1.62^{+0.01}_{-0.01}$	$2.52^{+0.08}_{-0.11}$	$4.91^{+0.21}_{-0.31}$	I	H
HBC 217	06 40 42.2	+09 33 37	6000±125	$0.82^{+0.01}_{-0.01}$	$1.75^{+0.10}_{-0.10}$	$6.89^{+1.13}_{-1.55}$	I	J
HBC 222	06 40 51.2	+09 44 46	6500±174	$0.97^{+0.06}_{-0.07}$	$1.70^{+0.12}_{-0.11}$	$8.24^{+1.77}_{-0.00}$		J
PDS 130	06 49 58.6	-07 38 52	10500±250	$1.90^{+0.03}_{-0.03}$	$2.74^{+0.10}_{-0.13}$	$3.08^{+0.22}_{-0.08}$	I	J
HD 68695	08 11 44.6	-44 05 09	9250±250	$1.35^{+0.02}_{-0.02}$	$2.08^{+0.06}_{-0.03}$	$8.02^{+0.91}_{-0.74}$	I	H
GSC 8581-2002	08 44 23.6	-59 56 58	9750±250	$1.52^{+0.01}_{-0.01}$	$2.40^{+0.00}_{-0.09}$	$5.12^{+0.86}_{-0.12}$	I	> Ks
PDS 33	08 48 45.7	-40 48 21	9750±250	$1.33^{+0.01}_{-0.01}$	< 2.10	< 9.19	I	J
PDS 297	09 42 40.3	-56 15 34	10750±250	$2.25^{+0.02}_{-0.02}$	$3.36^{+0.04}_{-0.10}$	$1.97^{+0.02}_{-0.05}$		> Ks
HD 87403	10 02 51.4	-59 16 55	10000±250	$2.83^{+0.04}_{-0.04}$	$5.54^{+0.23}_{-0.26}$	$0.40^{+0.05}_{-0.06}$		> Ks
HD 95881	11 01 57.6	-71 30 48	10000±250	$2.97^{+0.02}_{-0.02}$	$6.40^{+0.07}_{-0.19}$	$0.23^{+0.04}_{-0.03}$	II	J
HD 97048	11 08 03.2	-77 39 17	10500±500	$1.81^{+0.01}_{-0.01}$	$2.80^{+0.03}_{-0.03}$	$3.90^{+0.07}_{-0.60}$	I	J
HD 98922	11 22 31.7	-53 22 11	10500±250	$3.16^{+0.02}_{-0.02}$	$7.01^{+0.11}_{-0.02}$	$0.20^{+0.01}_{-0.01}$	II	J
HD 100453	11 33 05.5	-54 19 29	7250±250	$0.79^{+0.01}_{-0.01}$	$1.60^{+0.05}_{-0.04}$	$19.28^{+0.70}_{-0.68}$	I	J

Object	RA	DEC	$T_{\rm eff}$	Log(L_*)	M_*	Age	Meeus group	JHK group
	(h:m:s)	(d:m:s)	(K)	($L_\odot$)	($M_\odot$)	(Myr)		
HD 100546	11 33 25.3	-70 11 41	*9750±500*	$1.34^{+0.01}_{-0.01}$	$2.10^{+0.05}_{-0.03}$	$7.67^{+0.36}_{-0.67}$	I	J
HD 101412	11 39 44.4	-60 10 28	*9750±250*	$1.69^{+0.01}_{-0.01}$	$2.39^{+0.01}_{-0.02}$	$4.06^{+0.08}_{-0.01}$	II	J
HD 104237	12 00 04.9	-78 11 35	*8000±250*	$1.29^{+0.04}_{-0.04}$	$1.90^{+0.07}_{-0.05}$	$6.99^{+0.43}_{-0.87}$	II	J
HD 132947	15 04 56.0	-63 07 53	*10250±250*	$1.80^{+0.01}_{-0.01}$	$2.77^{+0.05}_{-0.01}$	$3.75^{+0.04}_{-0.81}$	II	> Ks
HD 135344B	15 15 48.4	-37 09 16	*6375±125*	$0.71^{+0.01}_{-0.01}$	$1.46^{+0.07}_{-0.04}$	$10.48^{+0.97}_{-0.49}$	I	J
HD 139614	15 40 46.4	-42 29 54	*7750±250*	$0.83^{+0.01}_{-0.01}$	$1.60^{+0.02}_{-0.00}$	$19.35^{+0.64}_{-0.00}$	I	H
HD 141569	15 49 57.7	-03 55 17	*9500±250*	$1.40^{+0.01}_{-0.01}$	$2.12^{+0.04}_{-0.01}$	$7.97^{+0.03}_{-0.03}$	II	> Ks
HD 142666	15 56 40.0	-22 01 40	*7250±250*	$1.13^{+0.01}_{-0.01}$	$1.75^{+0.03}_{-0.00}$	$8.73^{+0.08}_{-0.74}$	II	H
HD 142527	15 56 41.9	-42 19 24	*6500±250*	$1.35^{+0.01}_{-0.01}$	$2.20^{+0.05}_{-0.05}$	$4.40^{+0.49}_{-0.38}$	I	J
HD 143006	15 58 36.9	-22 57 16	*5500±125*	$0.54^{+0.02}_{-0.02}$	$1.74^{+0.10}_{-0.13}$	$5.10^{+1.89}_{-0.00}$	I	J
HD 144432	16 06 57.9	-27 43 10	*7500±250*	$1.21^{+0.01}_{-0.01}$	$1.82^{+0.03}_{-0.01}$	$7.98^{+0.02}_{-0.21}$	II	J
HR 5999	16 08 34.3	-39 06 19	*8500±250*	$1.97^{+0.08}_{-0.09}$	$3.19^{+0.21}_{-0.29}$	$1.98^{+0.33}_{-0.41}$	II	H
V718 Sco	16 13 11.6	-22 29 07	*7750±250*	$1.08^{+0.03}_{-0.04}$	$1.71^{+0.04}_{-0.02}$	$9.02^{+0.56}_{-0.11}$	II	Ks
HD 149914	16 38 28.6	-18 13 14	*9500±125*	$2.05^{+0.01}_{-0.01}$	$3.07^{+0.07}_{-0.05}$	$2.02^{+0.05}_{-0.02}$	II	> Ks
HD 150193	16 40 17.9	-23 53 45	*9250±250*	$1.36^{+0.01}_{-0.01}$	$2.25^{+0.00}_{-0.08}$	$6.00^{+1.00}_{-0.02}$	II	J
HD 158643	17 31 25.0	-23 57 46	*9500±150*	$2.25^{+0.01}_{-0.01}$	$3.60^{+0.07}_{-0.02}$	$1.35^{+0.16}_{-0.14}$	II	Ks
HD 163296	17 56 21.3	-21 57 22	*9000±250*	$1.19^{+0.04}_{-0.05}$	$1.91^{+0.12}_{-0.00}$	$10.00^{+9.50}_{-2.00}$	II	J
HD 169142	18 24 29.8	-29 46 50	*7250±125*	$0.76^{+0.01}_{-0.01}$	$1.55^{+0.03}_{-0.00}$	< 20.00	I	J
HD 176386	19 01 38.9	-36 53 27	*9750±125*	$1.64^{+0.01}_{-0.01}$	$2.63^{+0.00}_{-0.25}$	$3.88^{+0.57}_{-0.01}$		> Ks
HD 179218	19 11 11.3	+15 47 15	*9500±250*	$2.02^{+0.01}_{-0.01}$	$2.99^{+0.01}_{-0.04}$	$2.35^{+0.19}_{-0.16}$	I	H
WW Vul	19 25 58.8	+21 12 31	*8500±125*	$1.41^{+0.05}_{-0.06}$	$2.04^{+0.06}_{-0.05}$	$6.02^{+0.52}_{-0.20}$	II	J
PX Vul	19 26 40.3	+23 53 51	*6500±125*	$1.49^{+0.03}_{-0.03}$	$2.59^{+0.13}_{-0.18}$	$2.95^{+0.20}_{-0.64}$	II	J
V1295 Aql	20 03 02.5	+05 44 17	*9750±250*	$2.88^{+0.03}_{-0.03}$	$6.00^{+0.20}_{-0.21}$	$0.30^{+0.02}_{-0.02}$	II	J
HD 199603	20 58 41.8	-14 29 00	*7500±125*	$1.39^{+0.01}_{-0.01}$	$2.10^{+0.04}_{-0.05}$	$5.19^{+0.54}_{-0.19}$	II	> Ks
BP Psc	23 22 24.7	-02 13 42	*5250±125*	$0.40^{+0.17}_{-0.28}$	$1.65^{+0.24}_{-0.43}$	$4.89^{+8.26}_{-2.75}$	I	J

Notes. Columns 1, 2, and 3 show the names of the stars and their coordinates. Column 4 lists the effective temperatures, taken from Wichittanakom et al. (2020) when displayed in italics or from Guzmán-Díaz et al. (2021) otherwise. The values in the rest of the columns are taken from the latter work, listing the stellar luminosities, masses, ages, and the Meeus and JHK SED groups (see text).

Table A.2: Spectra used and stellar parameters derived in this work

Object	Instruments	Resolutions	$v \sin i$	$\log g$	[M/H]
	I_1/I_2	R_1/R_2	(km/s)	(dex)	(dex)
PDS 2	H/XS	80000/9900	15±1	4.23±0.05	≤ -0.10
HD 9672	H/H	115000/115000	200±10	3.97±0.07	0.20±0.10
HD 31648	U/XS	71000/9900	102±5	4.13±0.05	-0.25±0.13
UX Ori	XS/XS	9900/9900	225±11	3.75±0.12	0.00±0.10
HD 34282	XS/XS	9900/9900	105±5	4.43±0.10	≤ 0.00
HD 290380	U/U	71000/87400	75±4	3.98±0.05	0.00±0.10
HD 287823	XS/XS	9900/9900	27±1	4.25±0.11	-0.50±0.14
V346 Ori	U/XS	41000/9900	115±6	4.50±0.05	0.00±0.13
CO Ori	XS/XS	9900/9900	55±3	3.76±0.05	0.15±0.10
HD 35929	H/XS	80000/9900	60±3	3.50±0.05	0.12±0.10
HD 290500	XS/XS	9900/9900	80±4	3.79±0.25	0.00±0.10
HD 244314	XS/XS	9900/9900	55±3	4.08±0.05	0.00±0.10
HD 244604	XS/XS	9900/9900	100±5	3.95±0.18	0.50±0.10
RY Ori	XS/XS	3300/3300	57±3	4.00±0.05	0.00±0.14
HD 36917	XS/XS	9900/9900	110±6	4.29±0.07	0.20±0.10
HD 245185	XS/XS	9900/9900	115±6	4.22±0.06	-0.50±0.30
NV Ori	XS/XS	3300/3300	75±4	3.77±0.05	0.14±0.10
T Ori	U/XS	41000/9900	150±8	3.65±0.17	0.10±0.10
CQ Tau	XS/XS	3300/3300	98±5	4.13±0.05	≤ 0.00
HD 37258	U/XS	41000/9900	210±11	4.21±0.15	0.35±0.10
HD 290770	XS/XS	9900/9900	230±12	4.11±0.03	-1.00±0.33
BF Ori	-/XS	-/9900	37±2 (1)	3.87±0.34	0.20±0.13
HD 37357	U/XS	41000/9900	140±7	4.19±0.10	0.50±0.20
HD 290764	XS/XS	9900/9900	55±3	3.94±0.05	-0.15±0.10
V599 Ori	XS/XS	9900/9900	47±2	3.87±0.05	-0.35±0.10
V350 Ori	XS/XS	9900/9900	125±6	4.12±0.17	0.50±0.10
HD 38120	XS/XS	3300/3300	105±5	4.50±0.11	≤ 0.00
HD 39014	H/H	115000/115000	195±10	3.80±0.05	0.20±0.20
PDS 124	XS/XS	9900/9900	140±7	4.26±0.13	0.10±0.15
LkHa 339	XS/XS	9900/9900	130±7	4.15±0.14	0.50±0.12
HBC 217	U/U	48000/48000	36±1	3.95±0.05	-0.25±0.10
HBC 222	G/G	24000/24000	52±5	3.94±0.05	0.00±0.10
PDS 130	XS/XS	9900/9900	100±5	3.77±0.20	≥ 0.20
HD 68695	XS/XS	9900/9900	45±2	4.35±0.08	-0.50±0.10
GSC 8581-2002	XS/XS	9900/9900	155±8	3.90±0.05	0.00±0.10
PDS 33	XS/XS	9900/9900	140±7	4.41±0.08	-0.50±0.17
PDS 297	XS/XS	9900/9900	200±10	3.92±0.06	0.20±0.10
HD 87403	XS/XS	9900/9900	98±5	3.35±0.11	0.00±0.10
HD 95881	U/XS	41000/9900	70±4	3.19±0.11	0.00±0.10
HD 97048	U/XS	71000/9900	145±7	4.28±0.10	-0.50±0.13
HD 98922	U/XS	71000/9900	43±2	3.61±0.05	0.00±0.13
HD 100453	H/XS	115000/9900	50±3	4.47±0.05	-0.10±0.10

Object	Instruments I_1/I_2	Resolutions R_1/R_2	$v \sin i$ (km/s)	$\log g$ (dex)	[M/H] (dex)
HD 100546	U/XS	71000/9900	58±3	4.01±0.03	≤ -1.00
HD 101412	U/U	71000/107200	3±1	4.32±0.19	≤ 0.00
HD 104237	U/U	65000/74500	12±1	3.88±0.05	≤ 0.20
HD 132947	U/XS	41000/9900	118±6	3.95±0.11	0.20±0.10
HD 135344B	U/XS	71000/9900	70±4	4.15±0.05	0.00±0.13
HD 139614	XS/XS	9900/9900	32±2	4.45±0.05	-0.25±0.10
HD 141569	U/XS	71000/9900	220±11	4.09±0.08	-0.50±0.38
HD 142666	U/XS	41000/9900	65±3	3.99±0.05	0.00±0.10
HD 142527	U/XS	41000/9900	48±2	3.72±0.05	0.08±0.13
HD 143006	XS/XS	9900/9900	15±1	4.10±0.05	≤ -0.15
HD 144432	U/XS	41000/9900	77±4	4.00±0.05	0.15±0.10
HR 5999	U/XS	41000/9900	180±9	3.50±0.11	0.20±0.10
V718 Sco	H/XS	115000/5500	120±6	4.27±0.05	0.00±0.10
HD 149914	XS/XS	3300/3300	200±10	3.50±0.11	0.00±0.14
HD 150193	U/XS	41000/9900	107±5	4.08±0.14	0.20±0.10
HD 158643	XS/XS	5500/5500	222±11	3.50±0.11	0.20±0.10
HD 163296	U/XS	71000/9900	126±6	4.06±0.20	0.20±0.10
HD 169142	H/H	115000/115000	48±2	4.34±0.05	-0.50±0.33
HD 176386	U/XS	71000/9900	170±9	3.70±0.07	0.20±0.10
HD 179218	XS/XS	5500/5500	75±4	3.90±0.04	-0.50±0.17
WW Vul	U/U	41000/42300	190±10	3.65±0.01	≥ 0.20
PX Vul	U/U	41000/42300	78±4	3.63±0.05	0.00±0.10
V1295 Aql	XS/XS	9900/9900	25±1	3.69±0.11	≥ 0.10
HD 199603	U/U	41000/42300	90±5	3.89±0.05	0.00±0.10
BP Psc	H/H	115000/115000	40±2	4.16±0.05	0.20±0.16

Notes. Column 2 indicates the instruments I_1 and I_2 used to derive the projected rotational velocities (col. 4, see the references below for previous estimates of this parameter) and the widths of the Balmer lines and [M/H] values (related to cols. 5 and 6), respectively. XS refers to XSHOOTER, U to UVES, H to HARPS, and G to GIRAFFE. Column 3 shows the resolutions at ∼ 5000 Å of the spectra acquired with the aforementioned instruments.
References. (1) Mora et al. (2001).

Appendix B: Notes on individual objects

– **HD 31648:** Discrepancies in stellar parameters lead to different values of [M/H] in the literature. For instance, in Folsom et al. (2012) [M/H] = 0.23 is found for a T_{eff} = 8800 K and $\log g$ = 4.1. On the other hand, in Montesinos et al. (2009) the estimate is [M/H] = 0.0, being in this case T_{eff} = 8250 K and $\log g$ = 4.0. In this work, we derive a surface gravity similar to that of these works ($\log g$ = 4.13) but a lower effective temperature is used (T_{eff} = 8000 K), finally deriving [M/H] = -0.25.

– **HD 290380:** The observed spectrum analyzed has S/N below 100 (but high enough; $\geq$ 50).

– **HD 287823:** A value of $\log g$ = 4.25, which is similar to that provided by Wichittanakom et al. 2020, was fixed. The assumed uncertainty in this parameter was the mean error of $\log g$ from HAeBes with T_{eff} > 8000 K, which is 0.11.

– **BF Ori:** The $v \sin i$ of Mora et al. (2001) was considerered since the value of such parameter estimated from the process described in Sect. 3.1 does not fit properly the profiles of the photospheric lines of the selected regions in the interval 5000-7000 Å.

– **V599 Ori:** The observed spectrum analyzed has a S/N below 100 (but high enough; $\geq$ 70).

– **HD 38120:** The widths of the Balmer lines in the observed spectrum are larger than those estimated in the model generated with $\log g$ = 4.50. We assumed this value of $\log g$, and the same error as HD 287823 for this object.

– **HD 87048**: The value of $\log g$ for each [M/H] was estimated trough PARSEC V2.1s evolutionary tracks giving the T_{eff} from Wichittanakom et al. (2020), and the stellar mass and radius from Guzmán-Díaz et al. (2021). The considered error in $\log g$ is the same as HD 287823.

– **HD 95881**: The value of $\log g$ for each [M/H] was estimated trough PARSEC V2.1s evolutionary tracks giving the T_{eff} from Wichittanakom et al. (2020) and stellar mass and radius from Guzmán-Díaz et al. (2021). The considered error in $\log g$ is the same as HD 287823.

– **HD 141569:** The observed spectrum was challenging to analyze due to the scarcity of spectral lines, the high $v \sin i$, and S/N. Similar χ^2 were obtained in the fits with models generated at [M/H] equal to -0.5 and 0.0. Nevertheless, for this source we decided to fix [M/H] = -0.5, as this value is similar to the one derived from Kama et al. (2015), namely, [M/H] = -0.69.

– **HR 5999:** The widths of the Balmer series lines in the observed spectra are lower than those obtained in the models generated at $\log g$ = 3.5. The $\log g$ for each [M/H] was also estimated from PARSEC V2.1s evolutionary tracks, but no values below 3.5 were obtained. Therefore, a $\log g$ = 3.5 with the same error as HD 287823 were adopted.

– **HD 149914:** A $\log g$ = 3.5 was assumed based on the same reason described in HR 5999.

– **HD 158643:** A $\log g$ = 3.5 was assumed based on the same reason described in the case of HR 5999.

– **PX Vul:** The observed spectrum analyzed has a S/N below 100 (but high enough; $\sim$ 50).

– **BP Psc:** The observed spectrum analyzed has a S/N below 100 (but high enough; $\geq$ 70).